Fission barriers and half-lives of actinides in the quasimolecular shape valley

G. Royer, M. Jaffré, and D. Moreau
Laboratoire Subatech, UMR: IN2P3/CNRS-Université-Ecole des Mines, Nantes 44, France
(Received 25 May 2012; revised manuscript received 30 August 2012; published 19 October 2012)

The energy of actinide nuclei in the fusionlike deformation valley has been determined from a liquid-drop model, taking into account the proximity energy, the mass and charge asymmetries, and the shell and pairing energies. Double-humped potential barriers appear. The saddle point corresponds to the second maximum and to the transition from compact one-body shapes with a deep neck to two touching ellipsoids. The scission point, where the effects of the nuclear attractive forces between the fragments vanish, lies at the end of an energy plateau below the saddle point and corresponds to two well-separated fragments. The kinetic and excitation energies of the fragments come from the energy on this plateau. The shell and pairing effects play a main role to decide the most probable decay path. The heights of the potential barriers roughly agree with the experimental data and the calculated half-lives follow the trend of the experimental values. A shallow third minimum and a third peak appear in specific asymmetric exit channels where one fragment is close to a double magic quasispherical nucleus, while the other one evolves from oblate to prolate shapes.

DOI: 10.1103/PhysRevC.86.044326 PACS number(s): 25.85.Ca, 24.75.+i, 21.60.Ev, 21.10.Tg

I. INTRODUCTION

The observed properties of the ground-state and isomeric-state spectra of actinides suggest the existence of double-humped potential barriers. The heights of the inner and asymmetric outer fission barriers are almost constant (5–6 MeV) from Th to Am isotopes [1,2]. This is a severe test for theoretical models. Furthermore, analysis of the fission probability and of the angular distribution of the fragments indicates the existence of hyperdeformed states in a deep third well in several Th and U isotopes [3–5], confirming the pioneering work of Blons *et al.* [6] in ^{231,233}Th. The observed strongly enhanced low-energy α decay of several heavy actinide nuclei is also understood assuming the decay of a third hyperdeformed minimum, and the possibility that the third minimum is the true ground state of very heavy and perhaps superheavy nuclei has been also advocated [7]. Beyond the actinides, and very surprisingly, it is also necessary to advance fission barrier heights of 5–10 MeV to explain the successful formation in heavy-ion reactions of superheavy elements of charge 112–118, pointing out the determining influence of shell effects [8,9].

The fission shapes were first investigated a long time ago by minimizing the sum of the Coulomb and surface energies using mainly a development of the radius in Legendre polynomials. This leads naturally to fission paths through very elongated shapes with a shallow neck or no neck. By adding to the macroscopic liquid-drop model energy of these elongated one-body shapes, an oscillatory microscopic contribution, the Strutinsky's method [10], generated double-humped barriers allowing explaination of the fission isomer characteristics. On the other side, Myers and Swiatecki [11] proposed analytical formulas to calculate rapidly the shell and pairing energies for deformed shapes. Later, the asymmetric two-center shell model [12], the Hartree-Fock-Bogoliubov [13], and the relativistic mean-field theories [14] have also succeeded in obtaining different minima in the potential landscape where strongly deformed fission isomers can survive.

Within a generalized liquid-drop model (GLDM) taking into account both the proximity energy between close opposite surfaces and the mass and charge asymmetries, most of the symmetric and asymmetric fission [15–17], α and light nucleus emission [18,19], and fusion data [20], as well as the rotating super and highly deformed state characteristics [21,22], have been also reproduced in the fusionlike shape valley. It has been proved that there is a degeneracy between the energy of elongated shapes with a shallow neck and the energy of quasimolecular shapes, as well as between the values of the moment of inertia and quadrupole moment [23] in the two deformation paths. Consequently, the experimental data do not allow us to choose between them.

The purpose of this work is to focus on the actinide region remaining in the peculiar quasimolecular shape valley, taking into account the ellipsoidal deformations of the two different fission fragments, in order to investigate all possible mass and charge asymmetries in the framework of the GLDM, accounting for shell and pairing energies. The study is limited to quasimolecular shapes since these shapes are rarely investigated and are inaccessible in using the usual development of the nuclear radius.

II. POTENTIAL ENERGY OF A DEFORMED NUCLEUS

The energy of a deformed nucleus is the sum of the GLDM energy and the microscopic shell and pairing energies. The GLDM energy is given by [20]

$$E = E_V + E_S + E_C + E_{\rm prox}, \tag{1}$$

where the different terms are, respectively, the volume, surface, Coulomb, and nuclear proximity energies.

All along the fission path the proximity energy term $E_{\rm prox}$ takes into account the nuclear attractive forces between nucleons in the neck, in the case of a deformed one-body shape, or across the gap, in the case of two separated fragments. In

the quasimolecular shape valley, where the necks are narrow and well developed, this correction to the surface energy plays a main role in a large part of the fission path and especially around the touching point. For example, at the contact point between two spherical Kr and Ba nuclei the proximity energy reaches −43 MeV. The absence of this term in fusion studies leads to an unrealistic Coulomb peak. When the proximity energy is taken into account, the fusion barrier is smooth and the maximum corresponds to two separated nuclei maintained in unstable equilibrium by the balance between the repulsive Coulomb forces and the attractive nuclear proximity forces. In fission studies this term is very important when creviced and compact shapes are considered and is almost negligible for elongated shapes with a shallow neck. The proximity energy is defined as

$$E_{\rm prox}(r) = 2\gamma \int \Phi\left[D(r,h)/b\right] 2\pi h dh, \tag{2}$$

where r is the distance between the mass centers; Φ is the proximity function of Feldmeier [24]; h is the transverse distance varying from zero, for separated fragments or the neck radius for one-body shapes, to the height of the neck border; b is the surface width fixed at the standard value of 0.99 fm; and D is the distance between the opposite surfaces on a line parallel to the fission axis (see also Refs. [20,24]). Finally, the surface parameter γ is given by a geometric mean between the surface parameters of the two fragments,

$$\gamma = 0.9517\left(1 - k_s I_1^2\right)^{1/2}\left(1 - k_s I_2^2\right)^{1/2} \text{ MeV fm}^{-2}. \tag{3}$$

The selected one-body shape sequence simulating the fusionlike fission valley is shown in the upper part of Fig. 1. Two elliptic lemniscatoids are connected, allowing the development of a deep neck while keeping almost spherical ends [20]. The proximity energy is maximized in this deformation path.

For a given final asymmetry, there is a one-to-one correspondence between the distance r between the centers of the future fragments and the shape of the deformed nucleus [20].

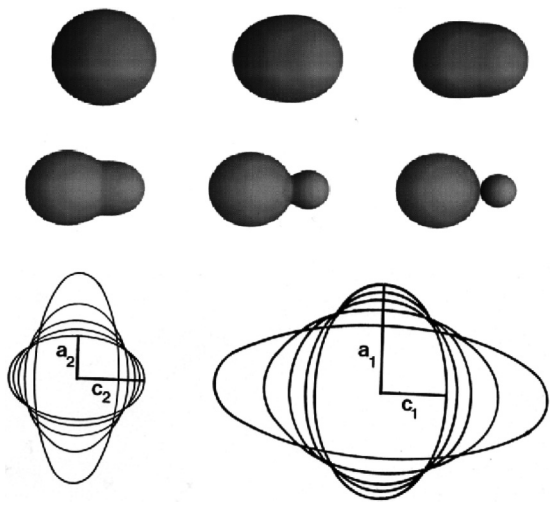

FIG. 1. Shape sequences describing the one-body shape evolution (for a given final asymmetry) and the two coaxial ellipsoid configurations. The fission axis is the common axis of revolution.

For one-body shapes, the first three contributions are expressed as

$$E_V = -15.494(1 - 1.8I^2)A \text{ MeV}, \tag{4}$$

$$E_S = 17.9439(1 - 2.6I^2)A^{2/3}\frac{S}{4\pi R_0^2} \text{ MeV}, \tag{5}$$

where I is the relative neutron excess and S is the surface of the deformed nucleus. The values of the surface energy coefficient and asymmetry surface energy coefficient are very close to those proposed by the Lund group and have never been changed since the first study [15],

$$E_C = 0.6e^2(Z^2/R_0)B_C. \tag{6}$$

The Coulomb shape-dependent function B_C is defined as

$$B_C = \frac{15}{16\pi^2 R_0^5}\int d\tau \int \frac{d\tau'}{|r - r'|}. \tag{7}$$

It has been determined within the method proposed by Cohen and Swiatecki [25] using the axial symmetry of the system and complete elliptic integrals [26],

$$B_C = 0.5\int (V(\theta)/V_0)(R(\theta)/R_0)^3 \sin\theta d\theta, \tag{8}$$

where $V(\theta)$ is the electrostatic potential at the surface and V_0 the surface potential of the sphere. The radius R_0 of the compound nucleus is given by

$$R_0 = (1.28A^{1/3} - 0.76 + 0.8A^{-1/3}) \text{ fm}. \tag{9}$$

This formula, proposed in Ref. [27], was derived from the droplet model and from the proximity energy values and simulates rather a central radius for which $R_0/A^{1/3}$ increases slightly with the mass. It has been shown that this GLDM can be used to reproduce accurately the fusion [20,22], fission [15,17], and cluster [19] and α [18] radioactivity data. Furthermore, the values of the parameters can be used to calculate the nuclear masses [28].

The radii of the two fragments are calculated assuming volume conservation. For two-body shapes, the coaxial ellipsoidal deformations of the two fragments have been considered [29] (see the lower part of Fig. 1). For a given distance r between the mass centers of the two fragments the system configuration depends on two parameters: the ratios s_i $(i = 1, 2)$ between the transverse semiaxis a_i and the radial semiaxis c_i of the fragments,

$$a_i = R_i s_i^{1/3}, \quad c_i = R_i s_i^{-2/3}. \tag{10}$$

The prolate deformation is characterized by $s \leqslant 1$ and the related eccentricity is $e^2 = 1 - s^2$, while in the oblate case $s \geqslant 1$ and $e^2 = 1 - s^{-2}$. The volume and surface energies are the sum of the contributions of each fragment. In the prolate case, the relative surface energy is given by

$$B_{\rm Si} = \frac{\left(1 - e_i^2\right)^{1/3}}{2}\left[1 + \frac{\sin^{-1}(e_i)}{e_i\left(1 - e_i^2\right)^{1/2}}\right] \tag{11}$$

and, in the oblate case,

$$B_{\rm Si} = \frac{\left(1+\epsilon_i^2\right)^{1/3}}{2}\left[1+\frac{\ln\left(\epsilon_i+\left(1+\epsilon_i^2\right)^{1/2}\right)}{\epsilon_i\left(1+\epsilon_i^2\right)^{1/2}}\right] \quad \epsilon_i^2 = s_i^2 - 1. \tag{12}$$

The Coulomb self-energy of the spheroid i reads

$$E_{C,\rm self} = \frac{3e^2 Z_i^2 B_{ci}}{5R_i}. \tag{13}$$

The relative self-energy is, in the prolate case,

$$B_{Ci} = \frac{\left(1-e_i^2\right)^{1/3}}{2e_i}\ln\frac{1+e_i}{1-e_i} \tag{14}$$

and, in the oblate case,

$$B_{Ci} = \frac{\left(1+\epsilon_i^2\right)^{1/3}}{\epsilon_i}\tan^{-1}\epsilon_i. \tag{15}$$

The Coulomb interaction energy between the two fragments is calculated as

$$E_{C,\rm int} = \frac{e^2 Z_1 Z_2}{r}[s(\lambda_1)+s(\lambda_2)-1+S(\lambda_1,\lambda_2)] \qquad \lambda_i^2 = \frac{c_i^2-a_i^2}{r^2}. \tag{16}$$

In the prolate case, $s(\lambda_i)$ is expressed as

$$s(\lambda_i) = \frac{3}{4}\left(\frac{1}{\lambda_i}-\frac{1}{\lambda_i^3}\right)\ln\left(\frac{1+\lambda_i}{1-\lambda_i}\right)+\frac{3}{2\lambda_i^2}, \tag{17}$$

while, for the oblate shapes,

$$s(\lambda_i) = \frac{3}{2}\left(\frac{1}{\omega_i}+\frac{1}{\omega_i^3}\right)\tan^{-1}\omega_i - \frac{3}{2\omega_i^2} \qquad \omega_i^2 = -\lambda_i^2. \tag{18}$$

$S(\lambda_1,\lambda_2)$ can be calculated within a twofold summation,

$$S(\lambda_1,\lambda_2) = \sum_{j=1}^{\infty}\sum_{k=1}^{\infty}\frac{3}{(2j+1)(2j+3)}\frac{3}{(2k+1)(2k+3)} \times \frac{(2j+2k)!}{(2j)!(2k)!}\lambda_1^{2j}\lambda_2^{2k}. \tag{19}$$

III. ANALYTICAL SHELL ENERGY

The shape-dependent shell corrections have been determined within the droplet model formulas [30] with slightly different values of the parameters. The shell energy is

$$E_{\rm shell} = E_{\rm shell}^{\rm sphere}(1-3.1\theta^2)e^{-\theta^2}. \tag{20}$$

The shell corrections for a spherical nucleus are given by

$$E_{\rm shell}^{\rm sphere} = 5.8\left\{[F(N)+F(Z)]/(0.5A)^{2/3}-0.28A^{1/3}\right\}\ \text{MeV}, \tag{21}$$

where, for $M_{i-1} < X < M_i$, M_i being the magic numbers,

$$F(X) = q_i(X-M_{i-1}) - 0.6\left(X^{5/3}-M_{i-1}^{5/3}\right) \tag{22}$$

and

$$q_i = 0.6\left(M_i^{5/3}-M_{i-1}^{5/3}\right)/(M_i-M_{i-1}). \tag{23}$$

The assumed highest proton magic number is 114 while, for the two highest neutron magic numbers, the values 126 and 184 have been retained,

$$\theta^2 = (\delta R)^2/a^2. \tag{24}$$

The distortion θa is the root-mean-square of the deviation of the nuclear surface from the sphere, a quantity which incorporates indiscriminately all types of deformation. The range a has been chosen to be $0.286r_0$. For the two-body shapes, the total shell energy is the sum of the shell corrections for each deformed fragment.

This algebraic method to calculate the shell effects is questionable but it gives, at least for ellipsoidal deformations, almost the same results as the Strutinsky's method. Therefore, this approach seems justified for the ellipsoidal fragments and around the ground state. For large deformed one-body shapes the shell effects obtained by the Strutinsky's method are generally higher.

IV. PAIRING ENERGY

The pairing energy has been calculated with the following expressions provided by the Thomas-Fermi model [31].

For odd Z, odd N, and $N = Z$ nuclei,

$$E_{\rm Pairing} = 4.8/N^{1/3} + 4.8/Z^{1/3} - 6.6/A^{2/3} + 30/A. \tag{25}$$

For odd Z, odd N, and $N \neq Z$ nuclei,

$$E_{\rm Pairing} = 4.8/N^{1/3} + 4.8/Z^{1/3} - 6.6/A^{2/3}. \tag{26}$$

For odd Z and even N nuclei,

$$E_{\rm Pairing} = 4.8/Z^{1/3}. \tag{27}$$

For even Z and odd N nuclei,

$$E_{\rm Pairing} = 4.8/N^{1/3}. \tag{28}$$

For even Z and even N nuclei,

$$E_{\rm Pairing} = 0. \tag{29}$$

It is assumed that the pairing energy of the compound nucleus is constant before the separation and it is the sum of the pairing energy of the two fragments after the separation.

V. POTENTIAL BARRIERS

The potential barriers determined in the fusionlike fission valley within the macroscopic part of the GLDM (i.e., without pairing and shell effects) and with the two sphere approximation for the fragments are plotted in Fig. 2 for the symmetric fission of β-stable nuclei. The proximity energy introduces progressively an inflection in the potential energy curve. For $A < 215$ there is one saddle point corresponding to two separated spherical fragments in unstable equilibrium due to the balance between the repulsive Coulomb forces and the attractive nuclear proximity forces. For $A > 215$, there are two maxima. The inner maximum is close to the sphere while the outer one presents always the same configuration; between them a second minimum occurs due to the proximity effects in the neck which strongly lower the deformation energy.

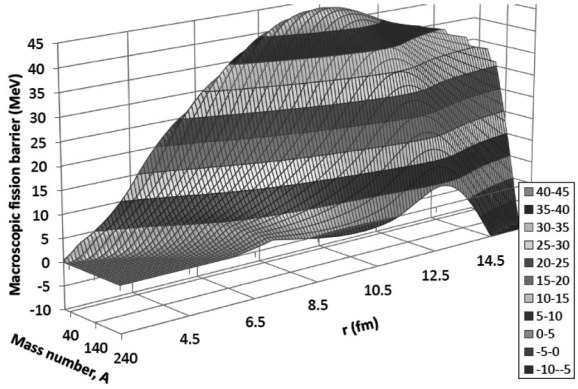

FIG. 2. Macroscopic barriers of the symmetric fission in the β-stability valley.

Naturally, these macroscopic double-humped barriers for actinides are not sufficient to reproduce the experimental data and the shell and pairing energies as well as the deformations of the fragments must be introduced.

The dependence of the deformation energy on the shape sequence and on the introduction of the microscopic corrections is displayed in Fig. 3 for an asymmetric fission path of the ^{240}Pu nucleus. The shell effects generate the slightly deformed ground state and contribute to the formation of the first peak. The proximity energy flattens the potential energy and the shell effects lead to the formation of a deep second minimum, lodging the observed superdeformed isomeric states. The value of the theoretical rigid moment of inertia, $2I/\hbar^2$, of the ground state is 133 MeV^{-1} relatively close to the experimental value of 140 MeV^{-1} [1]. The value of the experimental moment of inertia of the isomeric state is 299 MeV^{-1} while the theoretical one is 221 MeV^{-1}. The bottom of the second well is almost flat which may explain the difference between the two values.

The transition between one-body and two-body shapes is less smooth when the ellipsoidal deformations of the fragments are taken into account. Indeed, it corresponds to the transition (at $r = 11.6$ fm for ^{240}Pu) from a one-body quasimolecular shape with spherical ends, a very deep neck, and vanishing shell effects to two touching ellipsoidal fragments. The barrier height is reduced by several MeV. Later, the magic Sn nucleus remains almost spherical while the other fragment evolves from an oblate shape to a prolate shape but the proximity energy keeps close the two tips of the fragments. A plateau appears in the potential energy curve at larger distances around 10 MeV below the ground state. On this plateau the prolate deformation of the second fragment increases and the Coulomb and proximity energies diminish, the two fragments remaining in contact. The end of the plateau corresponds to the end of the contact between the two fragments and to a rapid transition from prolate to oblate or spherical shapes for the nonmagical fragment and to the vanishing of the proximity energy, with the two fragments going away.

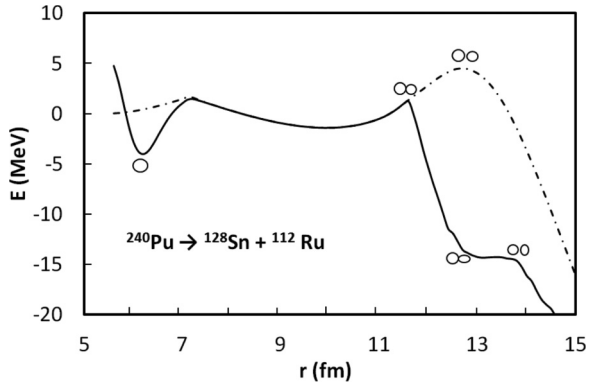

FIG. 3. Asymmetric fission barrier of a ^{240}Pu nucleus emitting a magic nucleus ^{128}Sn. The dashed-dotted curve gives the macroscopic energy within the two-sphere approximation for the two-body shapes while the solid line includes the ellipsoidal deformations of the fragments and the shell and pairing energies. r is the distance between the mass centers.

It must be pointed out that the macro-microscopic models [32] and the Hartree-Fock-Bogoliubov approaches [33] have difficulties smoothly connecting the two sheets of the potential energy surfaces corresponding, respectively, to one-body and two-body shapes. Furthermore, the models using elongated one-body shapes lead also generally to a second peak of the potential barrier, which is too high.

When the proximity energy is not taken into account, the scission point is often defined as the point where the rupture of the matter bridge between the nascent fragments occurs. In our approach, this point is the second peak of the double-humped barrier but this is not the real scission point. The introduction of the proximity energy changes the definition of the scission point. The scission point then is the point where the nuclear attraction between the fragments vanishes. It corresponds in our approach to the end of the plateau where the proximity energy becomes negligible and the scission configuration is that of two well-separated ellipsoids. The energy at the scission point is around 16 MeV lower than the energy at the external saddle point. As in other studies, a descent exists from the saddle point to the scission point. The final fragment shell effects play a main role during this descent, as underlined by Wilkins, Steinberg, and Chasman a long time ago [34]. Nevertheless, the fission fragment mass distribution is strongly connected with the relative half-lives of all the possible decays and, consequently, is mainly determined by the barriers along the fission path.

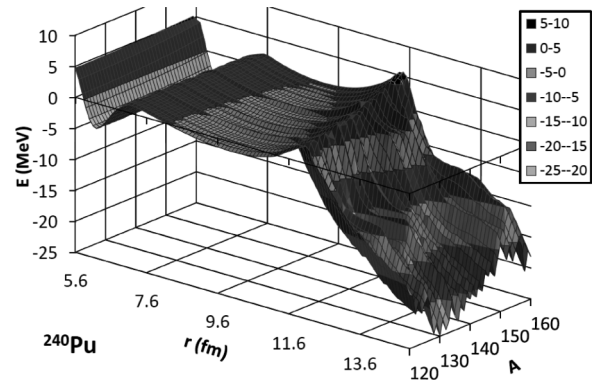

FIG. 4. Multiple-humped barriers for ^{240}Pu as a function of the heaviest fragment mass.

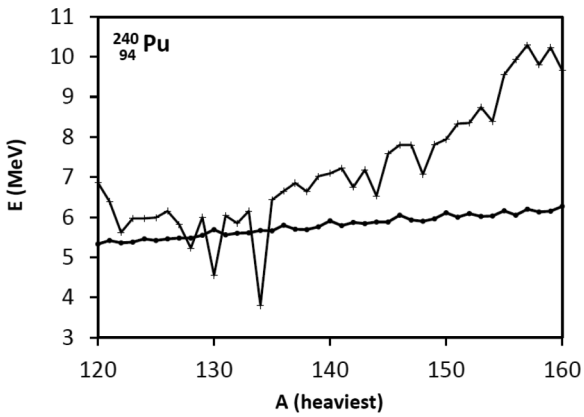

FIG. 5. Heights E_a and E_b of the inner (full circles) and outer (crosses) peaks of the fission barrier as a function of the mass of the heaviest fragment for ^{240}Pu.

The selected one-body shape sequence depends only on two parameters and does not allow the investigation of all the possible nuclear shapes. Its interest lies in the efficiency to very rapidly reach the contact point between spherical or deformed fragments and to check the largest possible nuclear proximity effects. This quasimolecular shape valley seems to be another possible candidate that allows the reproduction of the double-humped barriers of actinides.

In Fig. 4 the macro-microscopic double-humped barriers are displayed as a function of the mass of the heaviest fragment for the fission of the ^{240}Pu nucleus. For a given fragment mass, the charge which leads to the shortest decay half-life (see Sec. VI) has been retained. The height of the inner peak is almost constant since it depends on the assumed shell effects after the ground state of the decaying nucleus. The height of the external peak generally increases with the asymmetry but the shell and pairing corrections induce strong distortions from

TABLE I. Comparison between theoretical (t) and experimental (e) [1,2,4,6] barrier characteristics for actinide nuclei. E_a, E_b, and E_c are the first, second, and third peak heights while E_2 and E_3 are the energies of the second and third potential minima, relative to the ground-state energy (in MeV). The last column gives the energy of the plateau below the external barrier.

Reaction	E_a(t)	E_a(e)	E_2(t)	E_2(e)	E_b(t)	E_b(e)	E_3(th)	E_c(t)	Plateau energy
$^{230}_{90}$Th → $^{132}_{50}$Sn + $^{98}_{40}$Zr	4.9	–	4.5	–	7.7	–	6.8	8.4	190
$^{231}_{90}$Th → $^{132}_{50}$Sn + $^{99}_{40}$Zr	5.0	–	4.5	–	7.4	6.5	6.2	8.4	191
				–			e: 5.6	e: 6.3	
$^{233}_{90}$Th → $^{132}_{50}$Sn + $^{101}_{40}$Zr	5.25	–	4.4	–	6.5	6.8	5.1	7.65	189
				–			e: 5.2	e: 6.8	
$^{232}_{92}$U → $^{134}_{52}$Te + $^{98}_{40}$Zr	4.6	4.9	3.15	–	5.4	5.4	5.1	6.4	196
$^{234}_{92}$U → $^{134}_{52}$Te + $^{100}_{40}$Zr	5.0	5.6	3.2	–	4.8	5.5	4.3	6.3	195
				–			e: 3.1		
$^{235}_{92}$U → $^{131}_{50}$Sn + $^{104}_{42}$Mo	5.4	5.7	4.2	2.5	6.1	5.8	5.35	7.15	199
$^{236}_{92}$U → $^{130}_{50}$Sn + $^{106}_{42}$Mo	5.3	5.6	3.6	2.3	5.0	5.5	4.5	6.7	198
				–			e: 3.15		
$^{237}_{92}$U → $^{132}_{50}$Sn + $^{105}_{42}$Mo	5.8	6.1	4.6	2.5	6.2	5.9	4.9	7.1	199
$^{238}_{92}$U → $^{130}_{50}$Sn + $^{108}_{42}$Mo	5.6	5.7	3.8	2.6	5.1	5.7	4.6	6.5	200
$^{239}_{92}$U → $^{132}_{50}$Sn + $^{107}_{42}$Mo	5.9	5.8	4.4	1.9	5.6	6.0	4.0	6.2	197
$^{238}_{93}$Np → $^{132}_{50}$Sn + $^{106}_{43}$Tc	6.0	6.0	4.9	2.3	6.6	6.0	5.6	7.1	205
$^{238}_{94}$Pu → $^{132}_{52}$Te + $^{106}_{42}$Mo	5.2	5.6	2.3	2.7	5.1	5.4			210
$^{239}_{94}$Pu → $^{130}_{50}$Sn + $^{109}_{44}$Ru	5.6	6.2	3.4	2.6	4.75	5.5	4.7	5.6	207
$^{240}_{94}$Pu → $^{128}_{50}$Sn + $^{112}_{44}$Ru	5.5	5.7	2.6	2.4	5.2	5.1			205
$^{241}_{94}$Pu → $^{131}_{50}$Sn + $^{110}_{44}$Ru	6.0	6.0	3.8	1.9	4.8	5.5	4.2	5.1	207
$^{243}_{94}$Pu → $^{132}_{50}$Sn + $^{111}_{44}$Ru	6.2	5.9	4.0	1.7	5.0	5.4	3.7	4.5	208
$^{242}_{95}$Am → $^{131}_{50}$Sn + $^{111}_{45}$Rh	6.1	6.5	3.85	2.9	5.2	5.4	4.8	5.25	214
$^{243}_{95}$Am → $^{133}_{51}$Sb + $^{110}_{44}$Ru	6.0	5.9	3.2	2.3	4.1	5.4	3.3	4.0	214
$^{244}_{95}$Am → $^{132}_{50}$Sn + $^{112}_{45}$Rh	6.3	6.3	4.0	2.8	5.1	5.4	3.9	4.3	218
$^{243}_{96}$Cm → $^{122}_{48}$Cd + $^{121}_{48}$Cd	5.35	6.4	1.3	1.9	2.9	4.2			213
$^{245}_{96}$Cm → $^{130}_{50}$Sn + $^{115}_{46}$Pd	5.8	6.2	2.4	2.1	3.5	4.8			217
$^{248}_{96}$Cm → $^{130}_{50}$Sn + $^{118}_{46}$Pd	5.8	5.7	2.0	–	2.7	4.6			216
$^{250}_{97}$Bk → $^{130}_{50}$Sn + $^{120}_{47}$Ag	5.7	6.1	1.3	–	2.0	4.1			222
$^{250}_{98}$Cf → $^{125}_{49}$In + $^{125}_{49}$In	5.5	5.6	0.1	–	1.1	–			231
$^{256}_{99}$Es → $^{128}_{50}$Sn + $^{128}_{49}$In	5.2	4.8	−0.6	–	−0.2	–			232
$^{255}_{100}$Fm → $^{127}_{51}$Sb + $^{128}_{49}$In	5.4	5.7	−0.4	–	0.3	–			237

this global behavior. More precisely, the heights E_a and E_b of the two barriers are given in Fig. 5. The combination of the proton and neutron magic numbers, respectively, around 50 and 82, leads to a lowering of the second barriers for masses of the heaviest fragment around 130.

The "experimental" fission barriers are usually extracted from induced fission excitation functions at excitation energy above the barrier. Hence, they correspond roughly to the lowest possible theoretical fission barriers. Within the GLDM, for each studied actinide isotope, the half-lives of all the possible decays have been calculated (see Sec. VI). The decay giving the shortest half-life corresponds to the smallest action integral according to the method determining this half-life. This exit channel has been selected to compare the calculated and experimental energies of the maxima and minima of the fission barriers. The choice of this most probable fission path is difficult for some isotopes since there is a true degeneracy in energy between several paths. This problem comes from the fragment mass distribution which is very broad. The results are presented in Table I. The experimental and theoretical heights E_a and E_b of the two peaks roughly agree. The predicted value of the second minimum energy is often slightly too high. For the U, Pu, Am, and Cm isotopes, an asymmetric path is favored. One fragment is close to the doubly magic $^{132}_{50}$Sn nucleus and, consequently, keeps an almost spherical shape. This effect does not appear for Cf, Es, and Fm since for nuclei with $Z \sim 100$ the symmetric fission gives fragments with a charge close to the magic number 50. For the heaviest nuclei the external barrier disappears since the attractive proximity forces cannot compensate for the repulsive Coulomb forces any more.

The energy of the two deformed fragments at the end of the plateau below the multiple-humped barrier is given in the last column of Table I. It follows the trend of the experimental distribution of the total kinetic of the fragments but it overestimates the data of about 20–30 MeV. That might be explained partially by the energy stored by collective excitation modes such as vibration, rotation, charge polarization, and so on.

A third shallow minimum and a third peak appear in certain asymmetric decay paths when the heaviest fragment is a magic nucleus which preserves its almost spherical shape. The nonmagic fragment was born in an oblate shape ($s \sim 1.4$), due to the small distance between the mass centers at the transition between one-body and two-body shapes. When this distance increases, the ratio s decreases, because the proximity energy tends to keep the two tips of the fragments close. The lightest fragment remaining in contact with the other spherical fragment approaches the spherical shape and its shell energy increases to reach a maximum, which is at the origin of the third peak and corresponds to two touching different spheres. Before reaching this third peak a third shallow minimum appears. Its shape is hyperdeformed and asymmetric, in agreement with the experimental data [4]. Later, the proximity forces maintain the two fragments in contact and the shape of the smallest one evolves to prolate shapes ($s < 1$), with the corresponding shell corrections decreasing. In the symmetric mass exit path, the proximity and Coulomb energies counterbalance the smallest shell effects and induce an asymmetric shape; the two fragments remain in contact but one fragment is oblate while the other one is prolate. With increasing distance between the mass centers the two nuclei become prolate. There is no third barrier in the symmetric deformation paths. The still sparse and controversial data for the third barrier are roughly reproduced.

Clearly, the magicity of the proton and neutron numbers of the fragments plays a main role in discriminating between all the possible exit channels. Different hypotheses have been checked regarding the calculations of the pairing energy: pairing depending on the shape, pairing independent of the shapes but differing for one- and two-body shapes, and no pairing term. There are variations but the global consensus is about the same.

TABLE II. Comparison between experimental [2] and theoretical spontaneous fission half-lives of actinide nuclei.

Reaction	$T_{1/2,\exp(s)}$	$T_{1/2,\mathrm{theo}(s)}$
$^{232}_{92}\mathrm{U} \rightarrow {}^{134}_{52}\mathrm{Te} + {}^{98}_{40}\mathrm{Zr}$	2.5×10^{21}	4.8×10^{18}
$^{234}_{92}\mathrm{U} \rightarrow {}^{134}_{52}\mathrm{Te} + {}^{100}_{40}\mathrm{Zr}$	4.7×10^{23}	4.6×10^{19}
$^{235}_{92}\mathrm{U} \rightarrow {}^{131}_{50}\mathrm{Sn} + {}^{104}_{42}\mathrm{Mo}$	3.1×10^{26}	1.1×10^{24}
$^{236}_{92}\mathrm{U} \rightarrow {}^{130}_{50}\mathrm{Sn} + {}^{106}_{42}\mathrm{Mo}$	7.8×10^{23}	1.7×10^{22}
$^{238}_{92}\mathrm{U} \rightarrow {}^{130}_{50}\mathrm{Sn} + {}^{108}_{42}\mathrm{Mo}$	2.6×10^{23}	5.2×10^{23}
$^{238}_{94}\mathrm{Pu} \rightarrow {}^{132}_{52}\mathrm{Te} + {}^{106}_{42}\mathrm{Mo}$	1.5×10^{18}	2.1×10^{18}
$^{239}_{94}\mathrm{Pu} \rightarrow {}^{130}_{50}\mathrm{Sn} + {}^{109}_{44}\mathrm{Ru}$	2.5×10^{23}	9.9×10^{22}
$^{240}_{94}\mathrm{Pu} \rightarrow {}^{128}_{50}\mathrm{Sn} + {}^{112}_{44}\mathrm{Ru}$	3.7×10^{18}	2.3×10^{20}
$^{243}_{95}\mathrm{Am} \rightarrow {}^{133}_{51}\mathrm{Sb} + {}^{110}_{44}\mathrm{Ru}$	6.3×10^{21}	3.6×10^{22}
$^{243}_{96}\mathrm{Cm} \rightarrow {}^{122}_{48}\mathrm{Cd} + {}^{121}_{48}\mathrm{Cd}$	1.7×10^{19}	2.3×10^{16}
$^{245}_{96}\mathrm{Cm} \rightarrow {}^{130}_{50}\mathrm{Sn} + {}^{115}_{46}\mathrm{Pd}$	4.4×10^{19}	2.0×10^{20}
$^{248}_{96}\mathrm{Cm} \rightarrow {}^{130}_{50}\mathrm{Sn} + {}^{118}_{46}\mathrm{Pd}$	1.3×10^{14}	1.9×10^{18}
$^{250}_{98}\mathrm{Cf} \rightarrow {}^{125}_{49}\mathrm{In} + {}^{125}_{49}\mathrm{In}$	5.2×10^{11}	4.2×10^{11}
$^{255}_{99}\mathrm{Es} \rightarrow {}^{128}_{50}\mathrm{Sn} + {}^{127}_{49}\mathrm{In}$	8.4×10^{10}	5.5×10^{6}
$^{256}_{100}\mathrm{Fm} \rightarrow {}^{128}_{50}\mathrm{Sn} + {}^{128}_{50}\mathrm{Sn}$	1.0×10^{4}	1.1×10^{4}
$^{256}_{102}\mathrm{No} \rightarrow {}^{128}_{51}\mathrm{Sb} + {}^{128}_{51}\mathrm{Sb}$	110	1.9×10^{0}

VI. HALF-LIVES

Within this asymmetric fission model the decay constant is simply given by $\lambda = \nu_0 P$. The assault frequency ν_0 has been taken as $\nu_0 = 10^{20}$ s^{-1}. The barrier penetrability P is calculated within the action integral

$$P = \exp\left[-\frac{2}{\hbar} \int_{r_{\mathrm{in}}}^{r_{\mathrm{out}}} \sqrt{2B(r)(E(r) - E_{\mathrm{g.s.}})} dr \right]. \quad (30)$$

The inertia $B(r)$ is related to the reduced mass by

$$B(r) = \mu[1 + 24\exp(-3.25(r - R_{\mathrm{sph}})/R_0)], \quad (31)$$

where R_{sph} is the distance between the mass centers of the future fragments in the initial sphere, $R_{\mathrm{sph}}/R_0 = 0.75$, in the symmetric case. For shapes near the ground state, the inertia is largely above the irrotational flow value since a large amount of internal reorganization occurs at level crossings. For highly deformed shapes the reduced mass is reached asymptotically. The partial half-life is finally obtained by $T_{1/2} = \frac{\ln 2}{\lambda}$.

The experimental spontaneous fission half-lives and theoretical predictions for the assumed most probable exit channels are compared in Table II. There is a rough agreement with most of the experimental data on 26 orders of magnitude. Let us recall that the same GLDM and method to determine the half-lives have allowed an accurate reproduction of the α and cluster radioactivity half-lives [18,19].

VII. SUMMARY AND CONCLUSION

Exit channels of actinides via the quasimolecular shape valley have been investigated within a generalized liquid-drop model, including the nuclear proximity energy and microscopic corrections. Double-humped potential barriers and large deformed minima lodging possibly isomeric states appear. The external saddle point corresponds to the transition from one-body shapes to two touching ellipsoids. The scission point, where the effects of the nuclear attractive forces between the fragments vanish, lies at the end of an energy plateau below the saddle point. It corresponds to two well-separated fragments. The energy on this plateau gives the fragment kinetic energy plus an excitation energy. The barrier heights roughly agree with the experimental results on the double-humped fission barriers. The shell and pairing effects play a main role to decide the most probable decay path. The predicted half-lives follow most of the experimental data.

A shallow third minimum and a third peak appear in specific asymmetric exit channels where one fragment is close to a double magic quasispherical nucleus, while the other one evolves from oblate to prolate shapes.

[1] S. Björnholm and J. E. Lynn, Rev. Mod. Phys. **52**, 725 (1980).
[2] C. Wagemans, *The Nuclear Fission Process* (CRC Press, Boca Raton, FL, 1991).
[3] A. Krasznahorkay *et al*., Phys. Rev. Lett. **80**, 2073 (1998).
[4] A. Krasznahorkay *et al*., Phys. Lett. B **461**, 15 (1999).
[5] M. Hunyadi *et al*., Phys. Lett. B **505**, 27 (2001).
[6] J. Blons, C. Mazur, D. Paya, M. Ribrag, and H. Weigmann, Nucl. Phys. A **414**, 1 (1984).
[7] A. Marinov, S. Gelberg, D. Kolb, R. Brandt, and A. Pape, Int. J. Mod. Phys. E **12**, 1 (2003).
[8] P. Armbruster, Eur. Phys. J. A **37**, 159 (2008).
[9] V. Zagrebaev and W. Greiner, Phys. Rev. C **78**, 034610 (2008).
[10] V. M. Strutinsky, Nucl. Phys. A **95**, 420 (1967).
[11] W. D. Myers and W. J. Swiatecki, Ark. Fys. **36**, 343 (1967).
[12] M. G. Mustafa, U. Mosel, and H. W. Schmitt, Phys. Rev. C **7**, 1518 (1973).
[13] J. F. Berger, M. Girod, and D. Gogny, J. Physique Lett. **42**, 509 (1981).
[14] V. Blum, J. A. Maruhn, P. G. Reinhard, and W. Greiner, Phys. Lett. B **323**, 262 (1994).
[15] G. Royer and B. Remaud, J. Phys. G **10**, 1541 (1984).
[16] G. Royer and F. Haddad, Phys. Rev. C **51**, 2813 (1995).
[17] G. Royer and K. Zbiri, Nucl. Phys. A **697**, 630 (2002).
[18] G. Royer, J. Phys. G **26**, 1149 (2000).
[19] G. Royer and R. Moustabchir, Nucl. Phys. A **683**, 182 (2001).
[20] G. Royer and B. Remaud, Nucl. Phys. A **444**, 477 (1985).
[21] G. Royer, C. Bonilla, and R. A. Gherghescu, Phys. Rev. C **67**, 034315 (2003).
[22] G. Royer and J. Gaudillot, Phys. Rev. C **84**, 044602 (2011).
[23] J. Mignen, G. Royer, and F. Sebille, Nucl. Phys. A **489**, 461 (1988).
[24] H. Feldmeier, 12th Summer School on Nuclear Physics, Mikolajki, Poland, 1979 (unpublished).
[25] S. Cohen and W. J. Swiatecki, Ann. Phys. **22**, 406 (1963).
[26] J. Mignen and G. Royer, J. Phys. G: Nucl. Part. Phys. **16**, L227 (1990).
[27] J. Blocki, J. Randrup, W. J. Swiatecki, and C. F. Tsang, Ann. Phys. **105**, 427 (1977).
[28] G. Royer, M. Guilbaud, and A. Onillon, Nucl. Phys. A **847**, 24 (2010).
[29] G. Royer and C. Piller, J. Phys. G **18**, 1805 (1992).
[30] W. D. Myers, *Droplet Model of Atomic Nuclei* (Plenum, New York, 1977).
[31] W. D. Myers and W. J. Swiatecki, Nucl. Phys. A **601**, 141 (1996).
[32] P. Möller, A. J. Sierk, and A. Iwamoto, Phys. Rev. Lett. **92**, 072501 (2004).
[33] J. F. Berger, M. Girod, and D. Gogny, Nucl. Phys. A **502**, 85c (1989).
[34] B. D. Wilkins, E. P. Steinberg, and R. R. Chasman, Phys. Rev. C **14**, 1832 (1976).